Surface texturing of Mo–V–Te–Nb–Ox selective oxidation catalysts

Jakob B. Wagner[a,c], Olaf Timpe[a], Fazliana A. Hamid[b], Annette Trunschke[a,*], Ute Wild[a], Dang Sheng Su[a], Restu Kartiko Widi[b], Sharifah Bee Abd Hamid[b], and Robert Schlögl[a]

[a] Fritz-Haber-Institut der Max-Planck-Gesellschaft, Faradayweg 4-6, 14195 Berlin, Germany
[b] Combinatorial Technology and Catalysis Research Center (COMBICAT), Universiti Malaya, 50603 Kuala Lumpur, Malaysia
[c] Materials Chemistry, University of Lund, P.O. Box 124, SE-221 00 Lund, Sweden
To whom correspondence should be addressed: E-mail: trunschke@fhi-berlin.mpg.de

The paper concentrates on the study of Mo–V–Te–Nb oxide mixtures by electron microscopy combined with catalytic investigation of these materials in the partial oxidation of propane. Surface texturing of catalyst particles composed of two phases referred to in the literature as M1 and M2 is revealed by high-resolution transmission electron microscopy of high performing catalysts. The chemical composition of the catalyst surface is modified by treatment in water to obtain a significant increment in yield of acrylic acid. A chemical realization of the site isolation concept recurring on a supramolecular arrangement of catalyst and reactant rather than on atomic site isolation is suggested. A complex Mo–V–Te–Nb–Ox precursor phase carries nanoparticles made from a network of oxoclusters active as catalyst for the conversion of propane to acrylic acid. The designed synthesis of the multielement oxide bulk and of the surface structure with a different composition than the precursor phase improved the performance by a factor of 4.

KEY WORDS: catalyst model; heterogeneous catalysis; nanostructures; selective oxidation; surface analysis; Mo–V–Te–Nb oxide

1. Introduction

The selective oxidation of small alkane molecules with molecular oxygen is achieved with heterogeneous catalysts containing molybdenum oxide as key component. Structurally well-defined bulk orthorhombic MoO_3 is, however, fully inactive in these reactions [1,2], unless it is doped with other cations such as Sb, Bi, and V [3]. The cooperation of several phases, the availability of bulk lattice oxygen and the isolation of the active site in the crystallographic structural motif are key elements of the current paradigm on which many attempts are rested to improve the function of selective oxidation catalysts [4].

The resulting elemental and structural complexity of high performing catalysts is exemplified in the developments of Mo–V–Te–Nb [5–7] and Mo–V–W oxides [8] used in the oxidation of propane or propene, respectively, to acrylic acid. These reactions require the simultaneous function of the catalyst as activator of di-oxygen, as provider of selectively oxidizing oxygen atoms and as activator for stable C–H bonds. It is plausible that such complex functions require the exchange of electrons, protons and oxygen anions between different sites at the catalyst surface that must exhibit a highly adapted potential energy distribution ('landscape') to cater for a selective and time-efficient turnover of the reactants.

There is an ongoing debate about the origin of the high catalytic performance of Mo–V–Te–Nb oxides. It is proposed that a combination is required of two orthorhombic phases named M1 and M2, with the unit formula $Mo_{7.8}V_{1.2}NbTe_{0.937}O_{28.9}$ and $Mo_{4.31}V_{1.36}Nb_{0.33}Te_{1.81}O_{19.81}$, respectively [9]. These phases exhibit a large variation of M–O bond lengths and should thus provide the required specific electronic structure. The M1 phase (space group 32 (*Pba2*) with $a = 21.134$ Å, $b = 26.658$ Å, and $c = 4.0146$ Å) is closely related to the Mo_5O_{14} structure known to be active in the Mo–V–W systems, the M2 phase is an orthorhombic variant of the HTB structure (space group 25 (*Pmm2*) with $a = 12.6294$ Å, $b = 7.29156$ Å, and $c = 4.02010$ Å) [9].

There is a huge variation in phase composition and claimed performances of the nominally identical Mo - V– Te–Nb oxides in the open literature [5–7] and in the patent literature [10–13]. Inspection of the open structure of M1 being suitable for storing and transporting electrons and ions casts doubt on the claim of structural site isolation on the atomic level in view of the general similarity of the interconnection of polyhedra. The existence of a well-ordered surface resembling the bulk structure is questionable in terms of the surface free energy and even more considering the corrosive working conditions of 673 K in an atmosphere of air, saturated with steam and in the presence of a few vol% of reducing organic molecules.

The controversies could be resolved if the results from phase characterization are considered as indicating not the active phase but a precursor or decomposition product of a metastable arrangement of structural elements that can perform the sequence of elementary steps of the reaction. The active surface requires defects in its oxygen-terminated surface [14,15] for exposing metal sites to the reaction environment [16]. An array of oxoclusters linked by small metal-oxopolyhedra could provide

the transfer function for ions with low activation barriers [17–20] but requires a specific support structure to survive its dynamical rearrangement during catalytic operation. Led by this vision [21], crystalline Mo–V–Te–Nb oxide was optimized to function as support and as reservoir for the formation and stabilization of an active network of oxoclusters on the surface of the crystallites.

2. Experimental

Undiluted $Mo1V_{0.30}Te_{0.23}Nb_{0.125}O_x$ has been prepared according to the method described in the patent literature [11–13]. Dissolving 22.53 g ammonium heptamolybdate $(NH_4)_6Mo_7O_{24}$ $4H_2O$ (Merck) in 100 ml of bidistilled water at 333 K resulted in a colorless solution, which changed the color to yellow after adding 4.49 g solid ammonium metavanadate NH_4VO_3 xH_2O (Fluka). The mixture was heated up to 353 K to form a clear yellow solution. Subsequently, 6.74 g hexaoxotelluric acid $Te(OH)_6$ (Aldrich) was added at 353 K, yielding a deep red solution (Mo–V–Te solution). Afterwards, the Mo–V–Te solution was cooled down to 313 K and for the diluted systems, 14.36 g silica (Aerosil 300, Degussa), corresponding to about 50 wt% SiO_2 in the activated diluted catalysts, were added. Subsequently, the addition of 7.04 g ammonium niobium oxalate $(NH_4)_2Nb_2(C_2O4)_5$ (Aldrich) dissolved at 296 K in 30 ml bidistilled water led to precipitation and formation of an orange slurry. A Büchi spray dryer B-191 was used to spray-dry the slurry. An inlet temperature of 473 K was chosen. The delivery rate of the pump and the aspirator were attuned to an outlet temperature of 376 K. The spray-dried material was calcined in static air at 548 K (heating rate 10 K/min) for 1 h and subsequently treated in flowing helium at 873 K (heating rate 2 K/min) for another 2 h. After the final thermal treatment, the catalyst particles were dispersed in 0.5 l of distilled water. The dispersion was stirred at room temperature for up to 24 h and the conductivity was monitored. Thereafter, the solid catalyst material was separated from the liquid by centrifugation, and dried in a desiccator. The catalyst denominations are specified in the text. The activated samples are prepared for transmission electron microscopy (TEM) by dry-dispersion directly onto standard meshed copper grid coated with a holey carbon film. The samples are studied in a Philips CM 200 FEG TEM operated at 200 kV and equipped with a Gatan Image Filter and a CCD camera. Scanning electron microscopy (SEM) images are acquired with an S 4000 FEG microscope (Hitachi). The acceleration voltage is set to 5 kV and the working distance to 10 mm.

X-ray diffraction (XRD) measurements were done at room temperature on a STOE STADI-P focusing monochromatic transmission diffractometer equipped with a Ge(111) monochromator and a position sensitive detector. Cu-Kα radiation was used. The phase analysis was performed with the STOE Win XPOW software package (version 1.06; Stoe Darmstadt, Germany).

Conductivity measurements were carried out with a conductometer WTW LF 530 with conductivity cell LTA1. X-ray fluorescence measurements were carried out on a Seiko Instruments (SII) XRF machine.

XPS measurements were performed using a modified LHS/SPECS EA200 MCD system and Mg Kα radiation. Samples were used as loose powders to avoid any damaging of the surface layer. Compositions were obtained after subtracting satellites and stepped background and integration using empirical cross sections [22] of the raw data obtained in the pass energy mode (48 eV PE giving 0.9 eV FWHM of the Ag $3d_{5/2}$-intensity).

Catalyst screening and reaction study were carried out in a Nanoflow catalytic reactor with 12 fixed bed quartz tubular reactors (i.d., 4 mm; length, 225 mm), working at atmospheric pressure. Catalyst samples (0.24–0.45 mm particle size) were introduced into each reactor tube. The feed flow rate to each reactor was fixed at gas hourly space velocity (GHSV) of 1200 h^{-1} (at STP) with standard catalytic bed volume of 0.5 ml. The standard feed composition was propane/oxygen/nitrogen/ steam (1/2–2.2/18–17.8/9). The reaction was carried out at 673 and 683 K. The composition of all products was confirmed by two on-line gas chromatograph systems.

3. Results and discussion

In addition to standard Mo–V–Te–Nb–Ox catalysts, diluted samples have been prepared. As diluent, silica was added to the solution in the synthesis with the aim to separate the individual crystallites of the phases in such a way that sintering or Ostwald ripening of nanostructures is minimized under the harsh reaction conditions. The activated material was subsequently treated in water at 300 K in order to remove excess molybdenum oxide being active for detrimental total oxidation of propene [23]. We refer to this procedure as ''leaching''. The change in conductivity of the leaching solution was used as in situ monitor to select the leaching time. The increase of conductivity is consistent with the amount of molybdate released as was determined by XRF. In addition to molybdenum, small amounts of Te and V are found in the solution by XRF. Undiluted Mo–V–Te–Nb oxide was also subjected to this treatment. A rapid dissolution process and a slow re-organization process occur for both the diluted and undiluted samples. According to XPS (Table 1), the incongruent dissolution process leaves behind a chemically modified surface after prolonged leaching. Tellurium and vanadium are enriched near the surface in the diluted and leached sample (678). Moreover, fitting the V $2p_{3/2}$ peak (figure 1) reveals a higher fraction of V^{4+} (peak at 516.3 eV) to V^{5+} (peak at 517.3 eV) for the diluted samples after leaching.

XRD of the samples shows reflections of the M1 and M2 phase with a small amount of other phases detected. The intensity ratio of the corresponding M1 and M2 phases does not change during the leaching process. As an example, XRD of the undiluted leached sample is provided in figure 2.

Nanostructuring is verified by microscopic inspection allowing to study locally the relevance of the M1 structure for catalysis and to unravel the relative spatial arrangements of phases on several length scales using SEM and TEM techniques.

The SEM images of diluted Mo–V–Te–Nb oxide before and after leaching in figure 3 show that the distribution of the mixed oxide on the surface of the Aerosil particles is improved by leaching. SEM images of the leached Mo–V–Te–Nb oxide diluted with Aerosil, as shown in figure 4(a), reveal highly corrugated and porous 10 lm spherical agglomerates. The spheres originate from the spray-drying process of the precursor leading to an initially amorphous precursor. The porosity is due to the dispersion of the Aerosil, which is clearly observed in TEM images of the agglomerates (see upper part of figure 4(b)). The two overlapping rodshaped particles outlined in figure 4(b) are the multimetal oxides, which in general are 40–70 nm wide and exceed 100 nm in length.

Table 1
Near surface elemental compositionbased on XPS; atomic percentages normalized to Mo

Sample ID	Description	Mo	V	Te	Nb
679	Undiluted,leached in 1h,H_2O	1	0.21	0.24	0.15
671	Diluted	1	0.20	0.24	0.15
678	Diluted,leached, 24h,H_2O	1	0.24	0.42	0.11

High-resolution images of the multi-metal oxides reveal lattice fringes of the material being well-ordered within each crystallite. As the present crystalline material is known to be either the M1 phase or the M2 phase as observed from the XRD patterns (figure 2), it is possible to distinguish the single crystals by means of lattice fringes. Figure 4(c) and (d) show high-resolution images of the termination of M1 viewed in two different projections. In contrast to recent reports from DeSanto *et al.* [9,24], who claim no structural rearrangement to exist at the surface of the M1 and M2 phases, we clearly observe such structural rearrangements in both the M1 (figure 4(c), (d)) and M2 (not shown) phases. In general, the crystals are totally encapsulated by a 1–2 nm thick layer without long-range ordering, as shown in figurem4(d), where both the (210) and (001) planes of the M1-phase are terminated by the surface layer. It has to be stressed that the structural differences in the outermost region of the crystals are not due to contamination or to electron beam damage as the electron dose is kept at a minimum and no development of the layer is observed during longer exposure times in the electron microscope, see figure 5.

The termination of the well-defined bulk crystals is highly corrugated. The surface texturing illustrated in figure 6 can be described as ridges of up to 1 nm in thickness. Images acquired in a transmission electron microscope are projections, which impede the determination of the dimensions parallel to the electron beam. However, blurring of lattice fringes of the bulk M1 phase, as marked in figure 6, indicates
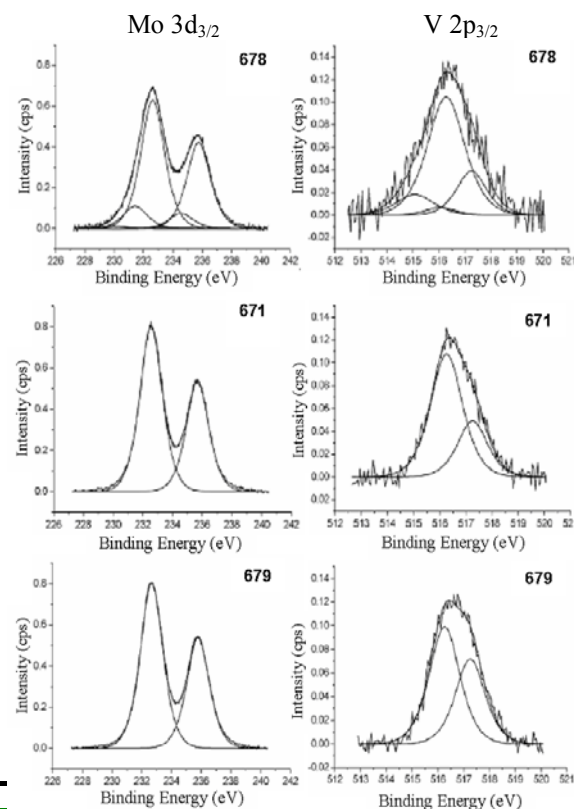

Mo 3d$_{3/2}$ V 2p$_{3/2}$

Figure 1. Fitting of the XPS spectra of Mo 3d$_{3/2}$ and V 2p$_{3/2}$. Sample ID as in Table 1.

the presence of surface textured regions or islands, with different structure than the bulk material, on top of the crystalline phase or in the bulk. To link the surface texturing to the altered chemical composition of the surface resolved with XPS, area confined EELS measurements are performed as shown in figure 7. Although the chemical composition of the surface layer is difficult to resolve due to low signal to noise ratio it is possible locally (1–2 nm) to reveal the existence of Mo, V and O at the surface as well as in the bulk material. The evidence of a multi-metal composition of the surface layers excludes the surface texturing to consist of unwanted excess molybdenum oxide and make it plausible to consider this layer as a relevant phase for the selective oxidation of propane.
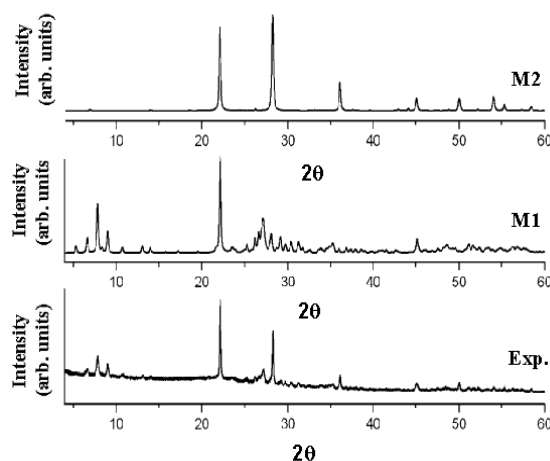

Figure 2. XRD of the undiluted sample 680 leached for 24 h together with simulated patterns for M1 and M2 phase
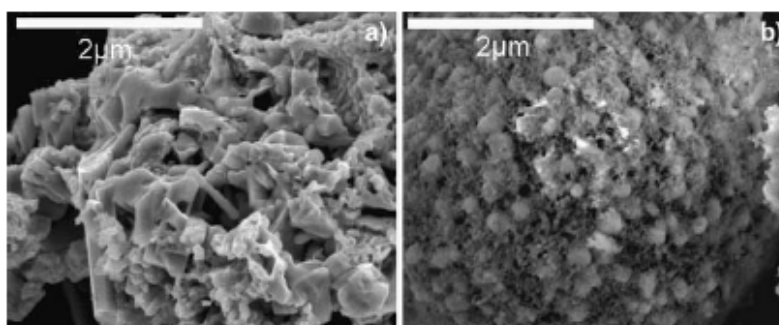
Figure 3. SEM images of the diluted sample. (a) Before leaching. (b) After 24 h leaching.

The high performing catalyst needs a support structure enabling rapid electron transfer and lattice oxygen $[O^{2-}]_L$ diffusion. This role could be played perfectly by the crystalline bulk Mo–V–Te–Nb oxide phases. The surface region is thought to expose the right selection of accessible metal-oxygen bond lengths, i.e. the right chemical potential landscape suitable for the conversion of propane and oxygen to acrylic acid. The beneficial function of surface nanostructuring and chemically modified surface composition is reflected in the catalytic performance.

Figure 8 shows the effects in a conversionselectivity diagram for two families of diluted and undiluted catalysts. The higher initial conversion of propane by the undiluted sample is due to a higher amount of metal oxide in the 0.5 ml sample tested in the reactor. The diluted sample is precipitated with the right surface texturing (chemical and geometrical), hence the higher initial selectivity. Short and long leaching, selected to compare the fast dissolution and the slow re-organization process, have pronounced but
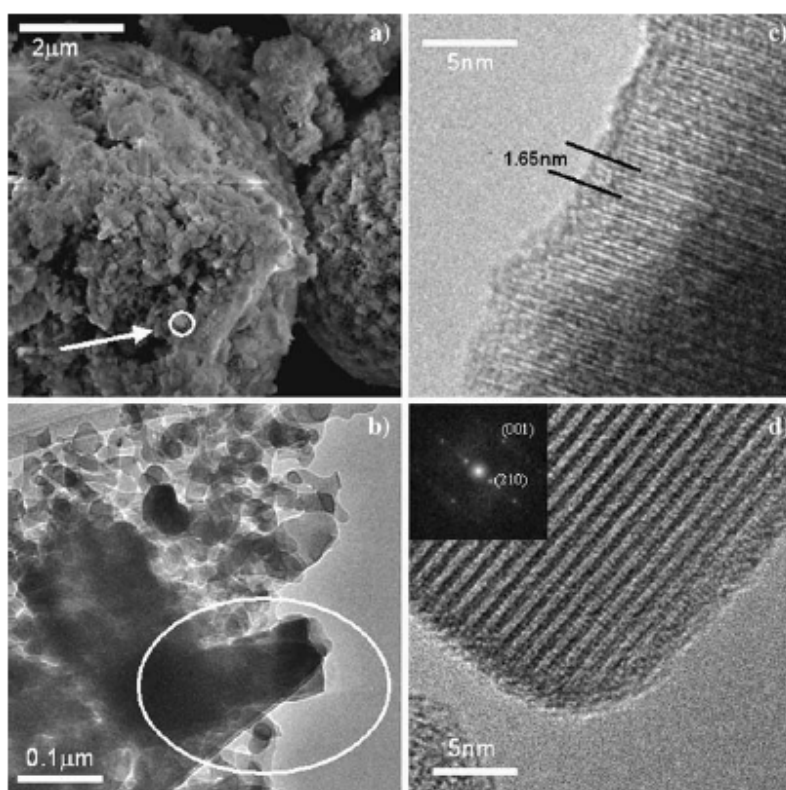

Figure 4. Morphology of sample agglomerates containing Aerosil after 24 h leaching: (a) SEM image. The size of the single Aerosil particles is indicated by a circle. (b) TEM image of the sample. (c) M1 phase viewed along the $[1\overline{1}0]$ zone axis. The lattice fringes ($d = 1.65$ nm) correspond to the (110) planes. (d) The crystalline phase coincides with structural data of the M1 phase viewed along the $\overline{1}20$ zone-axis revealing the (210) and (001) lattice planes as shown in the power spectrum (inset), i.e. the crystal is viewed along the $\overline{1}20$ zone-axis.

different effects on the performance. Diluted systems function best after long leaching times (678) whereas undiluted systems are better activated by short leaching times (679). Moreover, the largest effect on the conversion of propane is observed for the diluted samples, while significant changes are observed in the selectivity toward acrylic acid in the undiluted samples. The leaching of the diluted sample causes a

better distribution of the metal oxide on the surface of the Aerosil particle by dissolution and re-deposition processes that lead finally to an increase in the accessible metal oxide surface. A similar increase in the surface area is not possible in the undiluted sample and because of that mainly selectivity changes are observed due to the removal of less selective MoO_3 from the surface of the metal oxide
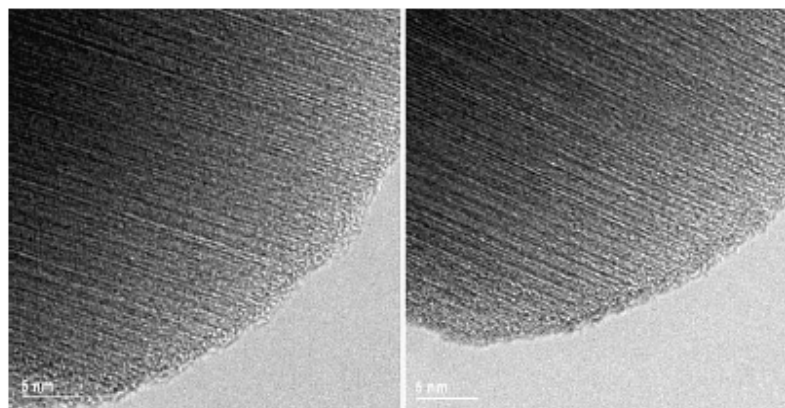
Figure 5. No beam damage is observed during longer exposure times under the conditions used. More than 10 min separate the two images.
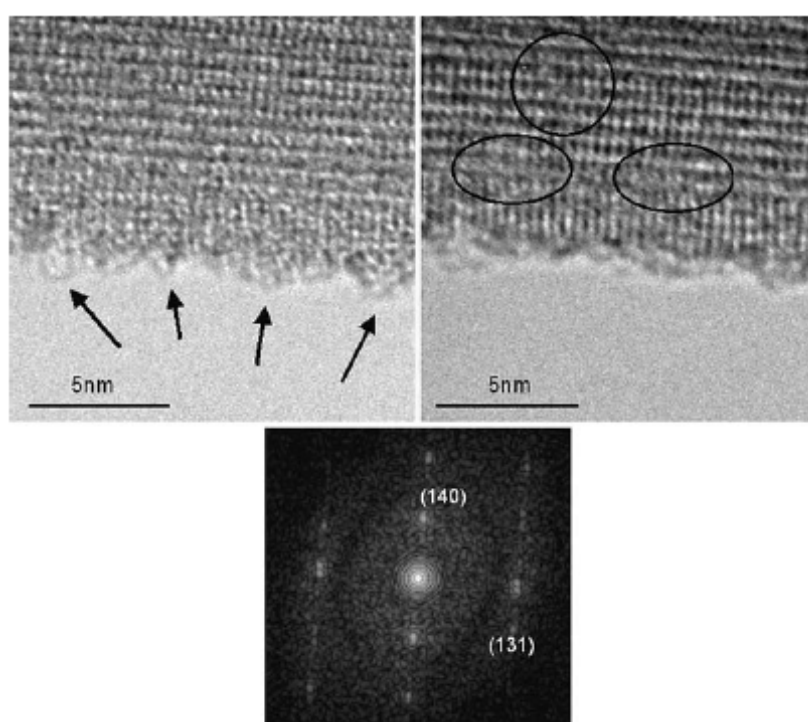

Figure 6. Surface texturing of M1 phase viewed along the $[4\overline{1}\overline{1}]$ zone-axis. Left: The surface texturing is shown in profile view (arrows). Right: Adjusting the defocus value reveals the surface texturing as blurring of the lattice fringe in top view (encircled).
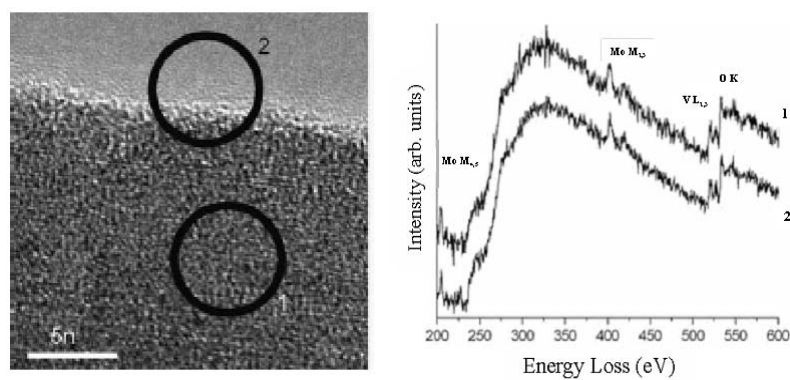

Figure 7. EELS of bulk material (1) and the surface (2) of the sample. The spectra showing the Mo $M_{4,5}$-, Mo $M_{2,3}$-, V $L_{2,3}$-, and O K ionization edges are offset for clarity.
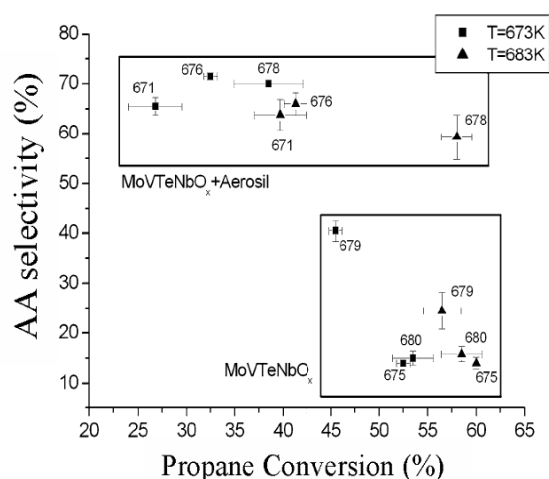
Figure 8. Selectivity towards acrylic acid versus propane conversion.Sample 671 and 675 are unleached, sample 676 and 679 are leached for1 h, and sample 678 and 680 are leached for 24 h. The temperaturesindicate reaction temperatures.

crystals. The yield of acrylic acid is very significantly improved by the two-fold modification of the system: The yield for the unleached and undiluted system is 8% whereas the best catalyst performs at a yield of 34%.

It is noted that despite the same bulk phase composition the effect of reaction temperature is different for diluted and undiluted systems indicating that the reaction kinetics and the catalyst structural dynamics may be very closely interrelated and that the overall performance of the system is determined more by the material dynamics rather than by the organic reaction cycle. This statement is in broad agreement with the Mars–van Krevelen paradigm [25] postulating that 'catalyst chemistry' and not 'reactant chemistry' should be ratelimiting in selective oxidation reactions.

The relevance of surface nanostructuring for the catalytic performance is rationalized in a phenomenological model sketched in figure 9, focusing on the potential for oxygen diffusion throughout the catalyst. A high-energy barrier for the transfer of lattice oxygen is located at the solid-gas interface (figure 9(a)). This barrier is responsible for the ability of a reducing atmosphere capable (due to its chemical potential) of reducing the solid to its (constituent) metals. In figure 9(b) a similar sketch is seen for a crystalline solid, terminated by a layer without long-range ordering. The barrier comprises now two interfaces. The inner boundary between long-range ordered and short-range ordered solids is small as still an oxygen ion is transported. Its movement in a loosely coupled polyhedral network should be even more facile than in a periodic rigid lattice and allow for a weakly activated transport through the surface to an acceptor molecule. Such 'assisted' ionic conductivity was also observed in other complex systems [26] and is also applied in other systems requiring facile ion transport through heterogeneous interfaces [27]. The relevance of metastable structurally unique interface layers for oxidation processes of metals was elucidated in detail
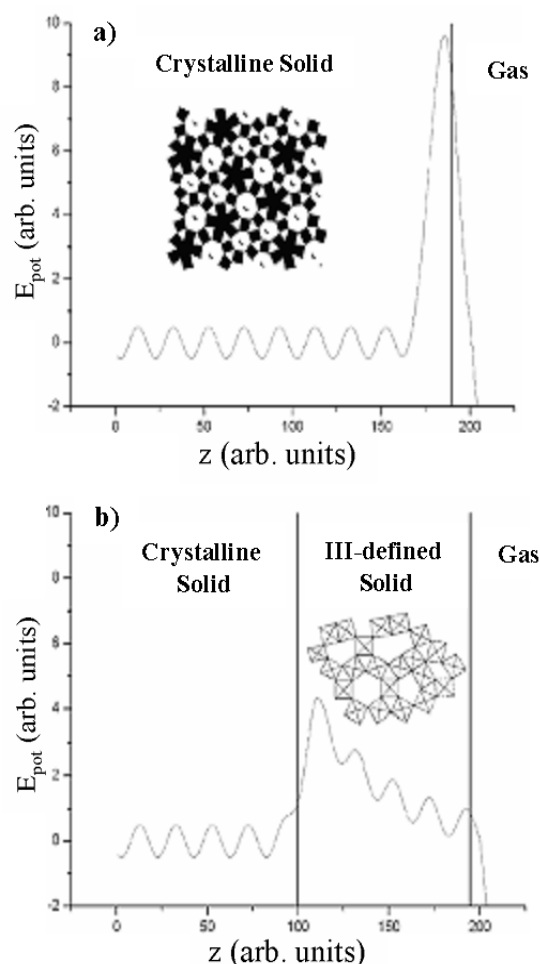

Figure 9. Effect of the co-existence of a short-range ordered 'transport overlayer' on the energetics of transport of lattice oxygen. (a) Single interface and (b) double interface. A similar picture holds for the redox behavior of the surface coupled to the transport of electrons.

by theoretical techniques [28]. If the short-range ordered solid comprises too large a part of the solid (e.g. due to too much leaching) the oxygen extraction energy becomes too low and will over oxidize the substrate. Too much oxygen could diffuse through the gas-solid interface. The co-existence of two differently organized solid phases is consistent with the concept of site isolation on a supramolecular level.

In summary, the study of the local geometric structure of high performing Mo–V–Te–Nb oxide catalysts reveals a structural different surface region terminating the bulk crystal, which is relevant for the catalytic performance. The structural complex bulk is the precursor to- and the support structure of the active phase and not the catalyst itself. This notion explains the extreme sensitivity of complex metal oxide catalysts, such as M1 and binary Mo oxides [29] to their synthetic history and provides a chemical meaning to the phenomenological concept of 'site isolation', which is difficult to rationalize in terms of a translational perfect crystal structure [4,6]. The concept presented here has also consequences for the functional understanding of other complex metal oxide catalysts that are relevant for the much desired

catalytic activation of small unfunctionalized alkanes, such as vanadyl pyrophosphate for butane oxidation [30–32]. Further improvement of these systems is now a question of optimizing the surface coverage and chemical constitution of the self-generated oxide nanostructure.

References

[1] J. Haber and E. Lalik, Catal. Today 33 (1997) 119.

[2] M.M. Lin, Appl. Catal. A 250 (2003) 305.

[3] B. Grzybowska, Top. Catal. 21 (2002) 35.

[4] R.K. Grasselli, Top. Catal. 21 (2002) 79.

[5] M.M. Lin, Appl. Catal. A 207 (2001) 1.

[6] R.K. Grasselli, Catal. Today 99 (2005) 23.

[7] J.M. Oliver, J.M. Lopez Nieto, P. Botella and A. Mifsud, Appl. Catal. A 257 (2004) 67.

[8] S. Knobl, G.A. Zenkovets, G.N. Kryukova, O. Ovsitser, D. Niemeyer, R. Schlögl and G. Mestl, J. Catal. 215 (2003) 177.

[9] P. DeSanto Jr., D.J. Buttrey, R.K. Grasselli, C.G. Lugmair, A.F. Volpe Jr., B.H. Toby and T. Vogt, Z. Kristallogr. 219 (2004) 152.

[10] M. Hatano and A. Kayou, European Patent No. 318,295 (1988).

[11] M. Hatano and A. Kayou, US Patent No. 5,049,692 (1991).

[12] T. Uchikubo, H. Nakamura, Y. Koyasu and S. Wajiki, US Patent No. 5,380,933 (1995).

[13] H. Hinago, S. Komada and A.K. Kogyo, US Patent No. 6,063,728 (2000).

[14] G. Ketteler, W. Weiss, W. Ranke and R. Schlögl, Phys. Chem. Chem. Phys. 3 (2001) 1114.

[15] B. Tepper, B. Richter, A.-C. Dupuis, H. Kuhlenbeck, C. Hucho, P. Schilbe, M.A. Bin Yarmo and H.-J. Freund, Surf. Sci. 496 (2002) 64.

[16] H. Over, Y.D. Kim, A.P. Seitsonen, S. Wendt, E. Lundgren, M. Schmid, P. Varga, A. Morgante and G. Ertl, Science 287 (2000) 1474.

[17] H. Werner, O. Timpe, D. Herein, Y. Uchida, N. Pfänder, U. Wild, R. Schlögl and H. Hibst, Catal. Lett. 44 (1997) 153.

[18] A. Müller, P. Kogerler and C. Kuhlmann, Chem. Commun. (1999) 1347.

[19] A. Müller, A. Beckmann, H. Bögge, M. Schmidtmann and A. Dress, Angew. Chem. Int. Ed. 114 (2002) 1210.

[20] A. Bielański and M. Najbar, Appl. Catal. A 157 (1997) 223.

[21] R. Schlögl and S.B.A. Hamid, Angew. Chem. Int. Ed. 43 (2004) 1628.

[22] D. Briggs, M.P. Seah, Practical Surface Analysis, (Wiley, New York, 1990).

[23] G. Mestl, J. Raman Spectrosc. 33 (2002) 333.

[24] P. DeSanto Jr., D.J. Buttrey, R.K. Grasselli, C.G. Lugmair, A.F. Volpe, B.H. Toby and T. Vogt, Top. Catal. 23 (2003) 23.

[25] P. Mars and D.W. Krevelen, Chem. Eng. Sci. 3 (1954) 41.

[26] B. Szymanic, R.G. Buckley, H.J. Trodahl and R.L. Davis, Solid State Ionics 109 (1999) 223.

[27] Y. Lui, J.Y. Lee and L. Hong, J. Power Sources 129 (2004) 303.

[28] K. Reuter, C. Stampfl, M.V. Ganduglia-Pirovano and M. Scheffler, Chem. Phys. Lett. 352 (2002) 311.

[29] J.B. Wagner, S.B. Abd Hamid, D. Othman, O. Timpe, S. Knobl, D. Niemeyer, D.S. Su and R. Schlögl, J. Catal. 225 (2004) 78.

[30] G.J. Hutchings, C.J. Kiely, M.T. Sananes-Schulz, A. Burrows and J.-C. Volta, Catal. Today 40 (1998) 273.

[31] F.J.C. Sanchez, J.A. Lopez-Sanchez, R.P. Wells, C. Rodes, A.-Z. Isfahani and G.J. Hutchings, Catal. Lett. 77 (2001) 189.

[32] C.J. Kiely, A. Burrows, S. Sajip, G.J. Hutchings, M.T. Sananes, A. Tuel and C.-J. Volta, J. Catal. 162 (1996) 31.